CrossMark
← click for updates

Decoration of Pt on Cu/Co double-doped CeO$_2$ nanospheres and their greatly enhanced catalytic activity†

Fan Wang,[b] Wang Li,[a] Xilan Feng,[a] Dapeng Liu*[a] and Yu Zhang*[a]

In this paper, we report an efficient strategy for the synthesis of Cu/Co double-doped CeO$_2$ nanospheres (Cu$_x$Co$_{1-x}$–CeO$_2$–Pt, $0 \leq x \leq 1$), which were fabricated *via* a simple water–glycol system. The following *in situ* surface decoration of Pt nanoparticles make these nanospheres highly active for the catalytic reduction of nitrophenol and CO oxidation. Detailed tests show that their catalytic performance strongly depends on the doping components and ion concentration of Cu and Co ions. The best samples of Cu$_{0.50}$Co$_{0.50}$–CeO$_2$–Pt and Cu$_{0.34}$Co$_{0.66}$–CeO$_2$–Pt demonstrate an excellent turnover frequency (TOF) of more than 450 h^{-1} after five cycles and retains about 99% conversion by using NH$_3$BH$_3$ as a reductant to reduce nitrophenol. Moreover, Cu$_{0.50}$Co$_{0.50}$–CeO$_2$–Pt possesses a much lower light-off and T_{100} (the temperature for 100% CO oxidation) temperature compared with the other catalysts.

Introductions

Among the metal oxides, CeO$_2$ has attracted great attention due to its excellent physicochemical properties including its good optical properties, mechanical strength, oxygen ion conductivity, and high thermal stability. CeO$_2$ has a fluorite-like cubic structure with each Ce^{4+} ion surrounded by eight O^{2-} ions in a face-centered cubic (fcc) arrangement, whereas each O^{2-} ion is tetrahedrally surrounded by four Ce^{4+} ions. Intrinsic oxygen vacancy defects can be rapidly formed and eliminated in the lattice of CeO$_2$, which favors mediation of lattice expansion and strain, and hence contributes significantly towards stable grain boundary structures. Hence, CeO$_2$ has been successfully employed in various applications such as in energy and magnetic data storage,[1] photocatalytic applications,[2–4] as sensors for CO,[5–9] H$_2$O$_2$,[10] NH$_3$,[11] and nitrophenol,[12,13] as a UV blocker,[14] in solar fuel synthesis,[15] water oxidation,[16,17] oxygen transfer,[18] fuel cells,[19,20] gates for metal-oxide semiconductor devices,[21] as a promoter in three-way catalysts for the elimination of polluted auto-exhaust gases from vehicles,[22–24] and so on.

The larger the amount of oxygen vacancies that CeO$_2$ possesses, the more efficient it will be for storing oxygen. Thus, it seems meaningful to control the generation of oxygen vacancies to improve its physicochemical properties.

Endeavours have been devoted to introduce dopants to improve the catalytic performance of CeO$_2$. It has been reported that its catalytic activity can be considerably enhanced by tuning the surface and interface structure through doping with isovalent/aliovalent cations into the CeO$_2$ lattice.[25–30] The isovalent cations that are frequently used are Ti^{4+}, Zr^{4+}, Hf^{4+}, and Sn^{4+}, while aliovalent cations used include Mn^{2+}, Ni^{2+}, Zn^{2+}, Ca^{2+}, Mn^{3+}, Sc^{3+}, Y^{3+}, Gd^{3+}, Sm^{3+}, Eu^{3+}, La^{3+}, *etc.* The substitution of isovalent dopants into the CeO$_2$ lattice decreases the oxygen vacancy formation energy due to structural distortion, whereas in the case of aliovalent dopants, the decrease in the defect formation energy is due to structural distortion as well as electronic modification, resulting in the generation of extra oxygen vacancies.[31,32] So once noble metals or metal oxides form hybrids with CeO$_2$, they often exhibit greatly enhanced catalytic activity, stability and selectivity.

Noble metal nanoparticles have been extensively studied for decades due to their high performance in many kinds of catalytic reactions. Smaller sized noble metal nanoparticles often have a larger fraction of exposed atoms on the particle surface, demonstrating better catalytic activity. Moreover, the strong synergistic effect between noble metals and the support greatly favors improvement of the catalytic performance,[33–38] especially for Pt–CeO$_2$ systems.[39–44] A recent report by Chowdhury *et al.*, reveals that doping can influence the surface acid–base properties of mesoporous CeO$_2$ and its catalytic behavior.[43] It is highly expected that incorporation of the cations into a ceria lattice structure will influence the redox properties of ceria in favour of synergistic interactions with noble metal nanoparticles towards enhanced activity for catalytic nitrophenol reduction and CO oxidation.

^{a}*Key Laboratory of Bio-Inspired Smart Interfacial Science and Technology of Ministry of Education, School of Chemistry and Environment, Beihang University, Beijing 100191, P.R. China. E-mail: liudp@buaa.edu.cn; jade@buaa.edu.cn*

^{b}*State Key Laboratory of Rare Earth Resource Utilization, Changchun Institute of Applied Chemistry, Chinese Academy of Science, Changchun, 130022 Jilin, China*

† Electronic supplementary information (ESI) available. See DOI: 10.1039/c5sc04069h

In this paper, an efficient strategy was developed for the synthesis of Cu_xCo_{1-x}–CeO_2–Pt hybrids. First, double-doped CeO_2 nanospheres were fabricated in a water–glycol mixed system, followed by a self-assembly process to *in situ* deposit Pt nanoparticles on the surface of the as-obtained double-doped CeO_2 nanospheres to form the final hybrids. Then, the as-obtained catalysts with different doping components were studied in detail to find the optimal doping ratios with the best catalytic performance for the reduction of 4-NP (4-nitrophenol) by NH_3BH_3 and the oxidation of CO. Furthermore, a detailed discussion has been made to clarify the role of the doping elements in the reduction of 4-NP and oxidation of CO, according to the analytical results.

Experimental section

Synthesis of CeO_2 nanospheres:

The synthesis of CeO_2 nanospheres was carried out by a previously reported method.[45] 500 mg of $Ce(NO_3)_3 \cdot 6H_2O$ and 200 mg of PVP were dissolved in 14 mL of ethylene glycol, and then 1 mL of deionized water was added to the above solution. After continuous stirring for 30 min, the clear solution was transferred into a Teflon-lined autoclave of 20 mL capacity and heated for 8 h at 160 °C. When the autoclave was cooled at room temperature, the products were collected and washed with deionized water and absolute alcohol several times. Finally, the products were dried at 60 °C overnight, and then calcined at 300 °C for 1 h at 1 °C min^{-1}.

Synthesis of Cu_xCo_{1-x}–CeO_2 nanospheres

500 mg of $Ce(NO_3)_3 \cdot 6H_2O$ and 200 mg of PVP were dissolved in 14 mL of ethylene glycol, and then 0.66 mL of 20 mg mL^{-1} $CuCl_2 \cdot 2H_2O$ and 0.34 mL of a 20 mg mL^{-1} $CoCl_2 \cdot 2H_2O$ solution were added to the above solution. The mixed solutions were transferred into a Teflon-lined autoclave of 20 mL capacity and heated for 8 h at 160 °C. When the autoclave was cooled to room temperature, the products were collected and washed with deionized water and absolute alcohol several times. Finally, the products were dried at 60 °C overnight, and then calcined at 300 °C at 1 °C min^{-1} for 1 h. The above products were labeled as $Cu_{0.66}Co_{0.34}$–CeO_2. Cu–CeO_2, $Cu_{0.50}Co_{0.50}$–CeO_2, $Cu_{0.34}Co_{0.66}$–CeO_2 and Co–CeO_2 were prepared in a similar process, except for changing the $CuCl_2 \cdot 2H_2O$/$CoCl_2 \cdot 2H_2O$ (v/v) to 1 mL $CuCl_2 \cdot 2H_2O$ and 0 mL $CoCl_2 \cdot 2H_2O$, 0.5 mL $CuCl_2 \cdot 2H_2O$ and 0.5 mL $CoCl_2 \cdot 2H_2O$, 0.34 mL $CuCl_2 \cdot 2H_2O$ and 0.66 mL $CoCl_2 \cdot 2H_2O$, and 0 mL $CuCl_2 \cdot 2H_2O$ and 1 mL $CoCl_2 \cdot 2H_2O$, respectively.

Synthesis of Cu_xCo_{1-x}–CeO_2–Pt hybrids

70 mg of Cu_xCo_{1-x}–CeO_2 nanospheres and 42 mg of PVP were first dissolved in 60 mL of ethylene glycol. After that, 0.84 mL of 0.02 M K_2PtCl_4 aqueous solution was added to the above solution. Then, the mixture was heated to 110 °C and was maintained at this temperature for 2 h. The product was collected by centrifugation and washed with deionized water several times and dried in an oven.

Characterization

The X-ray diffraction patterns of the products were collected on a Rigaku-D/max 2500 V X-ray diffractometer with $Cu_{K\alpha}$ radiation ($\lambda = 1.5418$ Å), with an operation voltage and current maintained at 40 kV and 40 mA. Transmission electron microscopic (TEM) images were obtained with a TECNAI G2 high-resolution transmission electron microscope operating at 200 kV. Inductively coupled plasma (ICP) analyses were performed with a Varian Liberty 200 spectrophotometer to determine the contents. X-ray photoelectron spectroscopy (XPS) measurements were taken on an ESCALAB-MKII 250 photoelectron spectrometer (VG Co.) with $Al_{K\alpha}$ X-ray radiation as the X-ray source for excitation. Decreases in the concentration of 4-NP were analyzed by UV-vis-NIR (SHIMADZU, UV-3600) spectrophotometer. The catalytic performances of the catalysts for CO oxidation were monitored on-line by gas chromatography (GC9800).

Catalytic tests

Chemical reduction of nitrophenol by NH_3BH_3: aqueous solutions of 4-NP (0.01 M) and NH_3BH_3 (0.1 M) were freshly prepared. 20 μL of the 4-NP solution and 100 μL of the NH_3BH_3 solution were added to a quartz cuvette containing 2 mL of water. Then, 20 μL of 5 mg mL^{-1} catalysts were injected into the cuvette to start the reaction. Since the spectrophotometer has a function to display the instant absorbance of a fixed absorption peak such as 400 nm, we can easily monitor the intensity of the absorption peak at 400 nm as a function of time. After each round of reaction, another 20 μL of 4-NP solution and 100 μL NH_3BH_3 aqueous solution were added to the reaction solution. This step was repeated 10 times to study the stability of the catalysts. The reduction of 4-NP by NH_3BH_3 can be briefly expressed as follows:
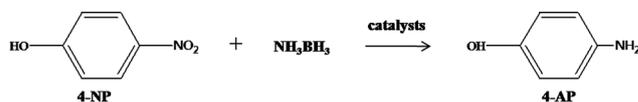
CO oxidation

20 mg of catalysts were put in a stainless steel reaction tube. The CO oxidation tests were performed under conditions in 1% CO and 20% O_2 in N_2 at a total flow rate of 30 mL min^{-1}, and a space velocity (SV) of 90 000 mL h^{-1} g_{cat}^{-1}. The composition of the gas was monitored on-line by gas chromatography.

Results and discussion

The synthesis of the Cu_xCo_{1-x}–CeO_2–Pt hybrid nanocatalysts involved two steps. Uniform Cu_xCo_{1-x}–CeO_2 nanospheres were first acquired by tuning the doping concentration of Co^{2+} and Cu^{2+}, and then they served as a support for the *in situ* deposition of Pt nanoparticles on their surface. Fig. 1 shows typical SEM images of the as-obtained Cu_xCo_{1-x}–CeO_2 samples, in which some detailed morphological and structural features can be found. All these samples are sphere-like with no obvious

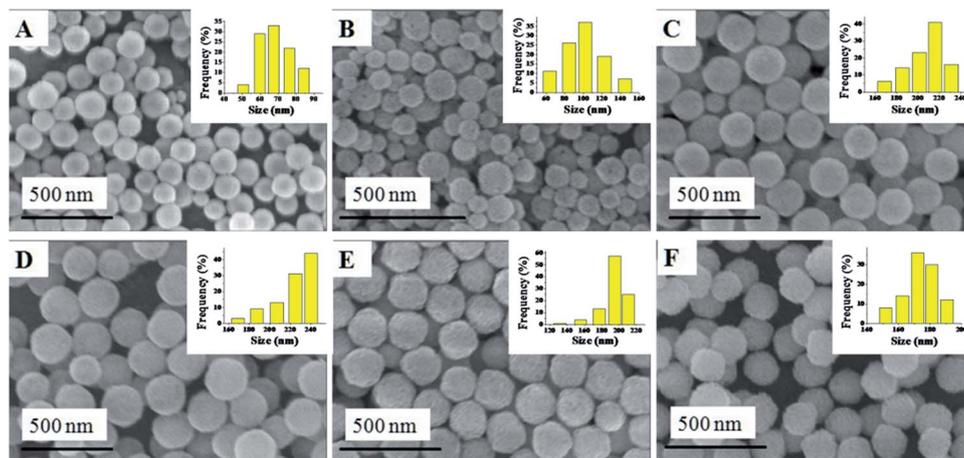Fig. 1 SEM images of (A) $Cu-CeO_2$; (B) $Cu_{0.66}Co_{0.34}-CeO_2$; (C) $Cu_{0.50}Co_{0.50}-CeO_2$; (D) $Cu_{0.34}Co_{0.66}-CeO_2$; (E) $Co-CeO_2$; (F) CeO_2.

fragments. Their size distributions are shown in Fig. 1 (inset) and are listed in Table S1.† Compared with the pure CeO_2 nanospheres of 174 nm, the Cu-rich ones are much smaller and are even less than 100 nm, while those Co-rich samples show a bigger size around 200 nm. Fig. 2 shows the SEM images of the as-obtained samples after the addition of K_2PtCl_4 aqueous solution and after being refluxed at 110 °C for 2 h. However, it is hard for us to distinguish the differences of the surface from the $Cu_xCo_{1-x}-CeO_2$ nanospheres, and no Pt particles can be found, indicating that the size of the deposited Pt nanoparticles should be very small in the $Cu_xCo_{1-x}-CeO_2-Pt$ hybrids. The sizes of the as-obtained $Cu_xCo_{1-x}-CeO_2-Pt$ hybrids are shown in Table S2.†

TEM characterization can tell us more information about the final $Cu_xCo_{1-x}-CeO_2-Pt$ hybrids. As shown in Fig. 3, these $Cu_xCo_{1-x}-CeO_2-Pt$ hybrids maintained their initial morphologies and inner nanostructures well. With a decrease in the amount of Cu^{2+} doping, the double-doped CeO_2 nanospheres obviously underwent a morphology transformation from hollow to core–shell, and then to be solid. The high-resolution TEM

image in Fig. 3 shows that each $Cu_xCo_{1-x}-CeO_2-Pt$ nanosphere is decorated by hundreds of ultra-small Pt nanoparticles (less than 2 nm) and the $Cu_xCo_{1-x}-CeO_2$ nanospheres are composed of closely packed CeO_2 nanoparticles with diameters of about 5 nm as primary building blocks. The clearly observed lattice spacing listed in Table S3† agrees well with that of Pt (200) (0.196 nm) and CeO_2 (111) (0.312 nm). The high angle annular dark field scanning transmission electron microscopy (HAADF-STEM) images of $Cu_{0.66}Co_{0.34}-CeO_2-Pt$ demonstrate the evenly distributed Cu, Pt and Co elements, as shown in Fig. 4.

In the X-ray diffraction (XRD) patterns of the $Cu_xCo_{1-x}-CeO_2-Pt$ and CeO_2-Pt nanospheres (Fig. 5), the diffraction peaks of all the products can be indexed to a pure phase of fcc CeO_2 structures (JCPDS no. 34-0394). The peaks at $2\theta = 28.549°$, 33.077°, 47.483°, 56.342°, 59.09°, 69.416°, 76.704° and 79.077° correspond to the characteristic (111), (200), (220), (311), (222), (400), (331) and (420) reflections, respectively. No signals related to impurities, such as cobalt oxide or copper oxide, can be found for all samples, indicating the homogeneous doping of
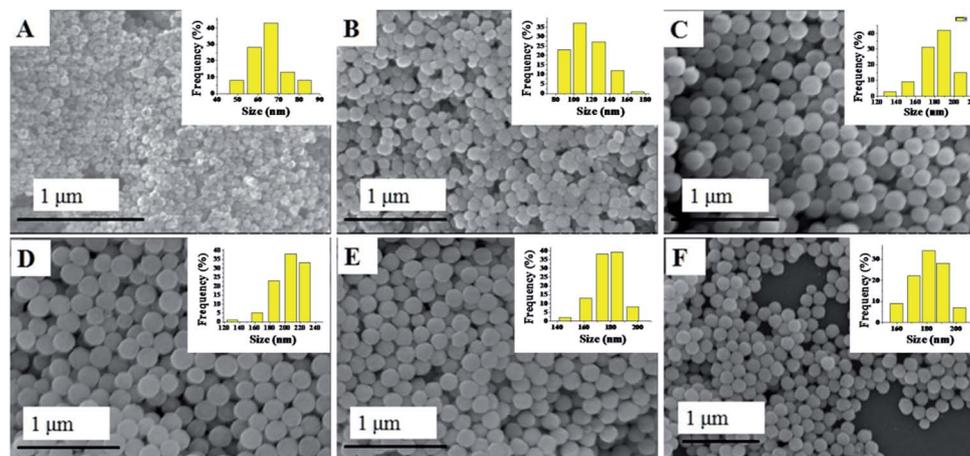

Fig. 2 SEM images of (A) $Cu-CeO_2-Pt$; (B) $Cu_{0.66}Co_{0.34}-CeO_2-Pt$; (C) $Cu_{0.50}Co_{0.50}-CeO_2-Pt$; (D) $Cu_{0.34}Co_{0.66}-CeO_2-Pt$; (E) $Co-CeO_2-Pt$; (F) CeO_2-Pt.
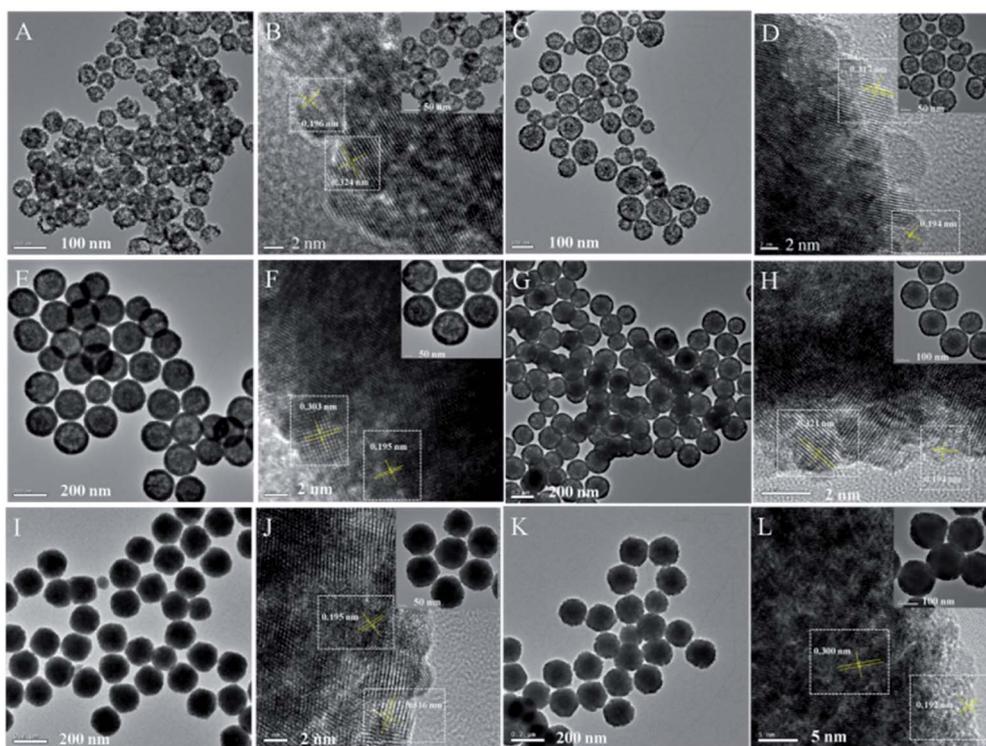
Fig. 3 TEM images of (A) and (B) Cu–CeO$_2$–Pt; (C) and (D) Cu$_{0.66}$Co$_{0.34}$–CeO$_2$–Pt; (E) and (F) Cu$_{0.50}$Co$_{0.50}$–CeO$_2$–Pt; (G) and (H) Cu$_{0.34}$Co$_{0.66}$–CeO$_2$–Pt; (I) and (J) Co–CeO$_2$–Pt; (K) and (L) CeO$_2$–Pt.
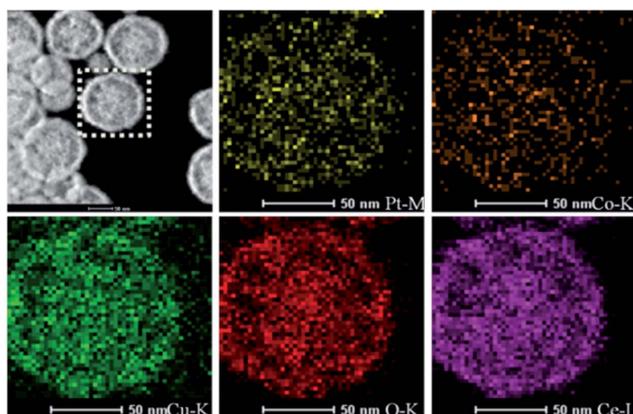
Fig. 4 HAADF-STEM images of Cu$_{0.66}$Co$_{0.34}$–CeO$_2$–Pt nanospheres.
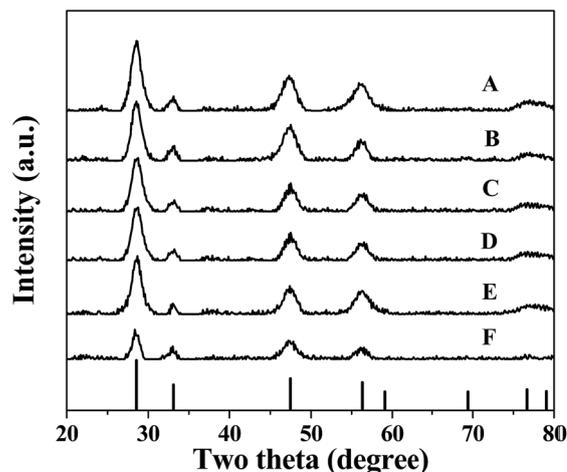
Fig. 5 XRD patterns of (A) Cu–CeO$_2$–Pt; (B) Cu$_{0.66}$Co$_{0.34}$–CeO$_2$–Pt; (C) Cu$_{0.50}$Co$_{0.50}$–CeO$_2$–Pt; (D) Cu$_{0.34}$Co$_{0.66}$–CeO$_2$–Pt; (E) Co–CeO$_2$–Pt; (F) CeO$_2$–Pt.

Cu and Co ions in the CeO$_2$ solid solutions. The contents of the elements Cu, Co, Ce and Pt for the Cu$_x$Co$_{1-x}$–CeO$_2$–Pt nanospheres were then determined by ICP-MS analysis and are listed in Table S4.† It can be seen that the loading amounts of Pt (mol%) are less than 1.4% if Cu^{2+} is introduced, however, in the absence of Cu^{2+}, this percentage increased to 4.1% for Co–CeO$_2$–Pt and 4.8% for CeO$_2$–Pt, which were much higher than the others. On the contrary, Co^{2+} doping has little effect on the deposition amount of Pt.

XPS analysis was employed to determine the surface elements and their valence states of the Cu$_x$Co$_{1-x}$–CeO$_2$–Pt and CeO$_2$–Pt nanospheres (Fig. 6). All of the samples show

characteristic peaks at the binding energies of 71.3 eV (Pt 4f$_{7/2}$) and 74.7 eV (Pt 4f$_{5/2}$) of the element Pt, and the two peaks at 882.8 and 899.5 eV correspond well to the Ce 3d$_{5/2}$ and Ce 3d$_{3/2}$ spin–orbit peaks of CeO$_2$. As previously reported, the XPS spectrum of Co 2p shows two major peaks at 795.5 and 780.4 eV, corresponding to Co 2p$_{1/2}$ and Co 2p$_{3/2}$ spin–orbit coupling, respectively.[46] Two major peaks lying at 932.2 and 954.2 eV are characteristic signals of Cu^{2+} with Cu 2p$_{3/2}$ and Cu 2p$_{1/2}$ orbits,
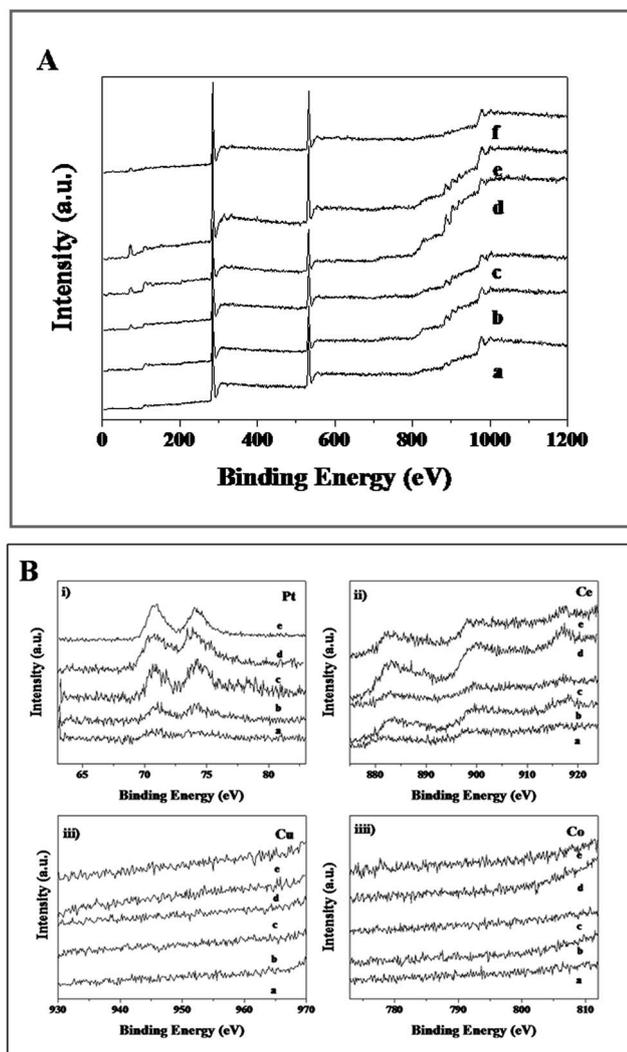
Fig. 6 (A) XPS spectra of (a) Cu−CeO$_2$−Pt, (b) Cu$_{0.66}$Co$_{0.34}$−CeO$_2$−Pt, (c) Cu$_{0.50}$Co$_{0.50}$−CeO$_2$−Pt, (d) Cu$_{0.34}$Co$_{0.66}$−CeO$_2$−Pt, (e) Co−CeO$_2$−Pt, (f) CeO$_2$−Pt. (B) XPS spectra of (a) Cu−CeO$_2$−Pt; (b) Cu$_{0.66}$Co$_{0.34}$−CeO$_2$−Pt; (c) Cu$_{0.50}$Co$_{0.50}$−CeO$_2$−Pt; (d) Cu$_{0.34}$Co$_{0.66}$−CeO$_2$−Pt; (e) Co−CeO$_2$−Pt.

respectively.[46] Unfortunately, due to the low doping content of Co and Cu in Cu$_x$Co$_{1−x}$−CeO$_2$−Pt, no Co and Cu signals can be detected in all the samples. However, in combination with the HAADF-STEM characterization and ICP results, the successful formation of Cu$_x$Co$_{1−x}$−CeO$_2$−Pt hybrids can be confirmed.

In the following, the reduction of 4-NP to 4-AP by NH$_3$BH$_3$ was selected to evaluate the catalytic performance of the as-obtained Cu$_x$Co$_{1−x}$−CeO$_2$−Pt and CeO$_2$−Pt samples. As is known, 4-NP exhibits a strong characteristic absorption peak at 317 nm while at pH < 7, but it will be ionized as the alkalinity of the solution increases, resulting in a spectral shift to 400 nm.[35] In our case, the absorption peak of 4-NP remained at 317 nm despite adding NH$_3$BH$_3$ solution, indicating that the NH$_3$BH$_3$ molecules were stable enough in water in the absence of the catalysts.[34] However, after addition of the Cu$_x$Co$_{1−x}$−CeO$_2$−Pt hybrids, the absorption intensity at 400 nm gradually increased.

The color of the reaction system changed from bright yellow to colorless. Since NH$_3$BH$_3$ was in a large excess relative to 4-NP, its concentration could be considered as constant during the reaction period. Thus, the reduction rate can be evaluated by pseudo-first-order kinetics with respect to 4-NP. Fig. 7A shows ln(C/C_0) *versus* reaction time t, which was obtained from the relative intensity ratio of the absorbance (A/A_0) at 400 nm. Here, C_0 and C represent the initial and instantaneous concentrations of 4-NP, respectively; and k and t stand for the rate constant and the reaction time in turn. As all of these plots followed first-order reaction kinetics very well, the value k can be calculated from the equation ln(C/C_0) = kt (Table 1). The catalytic activity of the six samples follows this sequence: Cu$_{0.66}$Co$_{0.34}$−CeO$_2$−Pt > Cu$_{0.50}$Co$_{0.50}$−CeO$_2$−Pt > Cu−CeO$_2$−Pt > Cu$_{0.34}$Co$_{0.66}$−CeO$_2$−Pt > Co−CeO$_2$−Pt > CeO$_2$−Pt, showing a strong dependence on the composition of Cu and Co. Furthermore, the turnover frequency (TOF), defined as moles of the reactant 4-NP converted per mole of active metal in the catalyst per hour was also calculated
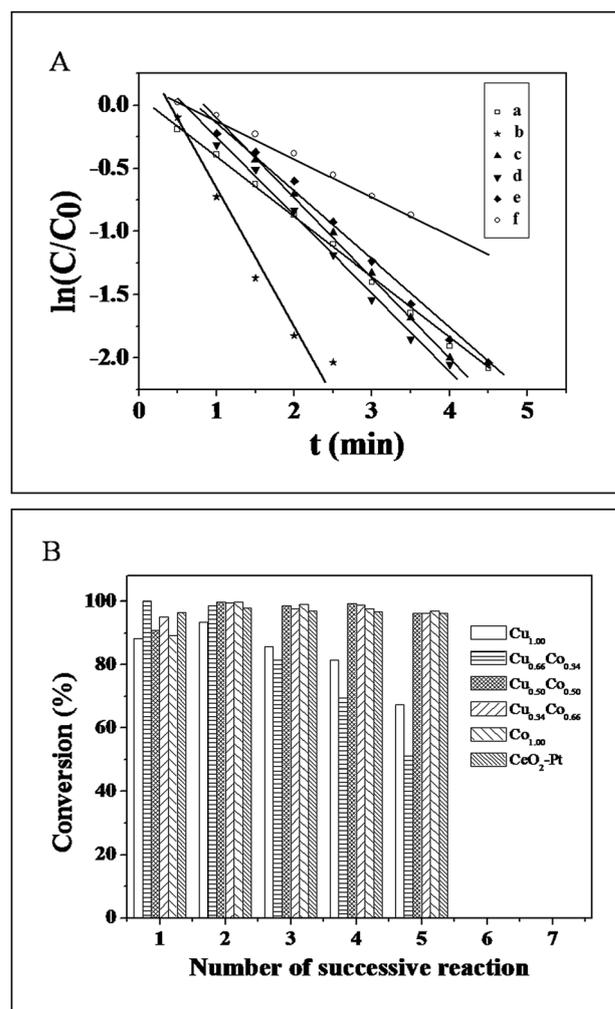
Fig. 7 (A) ln(C/C_0) *versus* t for the reduction of 4-NP catalyzed by (a) Cu−CeO$_2$−Pt; (b) Cu$_{0.66}$Co$_{0.34}$−CeO$_2$−Pt; (c) Cu$_{0.50}$Co$_{0.50}$−CeO$_2$−Pt; (d) Cu$_{0.34}$Co$_{0.66}$−CeO$_2$−Pt; (e) Co−CeO$_2$−Pt; (f) CeO$_2$−Pt. (B) Conversion in successive reaction cycles of Cu$_x$Co$_{1−x}$−CeO$_2$−Pt and CeO$_2$−Pt.

Table 1 Comparison of the rate constant k, TOF and conversion for 4-NP reduction with Cu_xCo_{1-x}–CeO_2–Pt and CeO_2–Pt catalysts[a]

Sample	k (s^{-1})	M_{Pt} (mmol)	$M_{4\text{-}NP}$ (mmol)	t (min)	TOF (h^{-1})	P (%)	Ref
$Cu_{1.00}$–CeO_2–Pt	0.451	3.35×10^{-6}	2.00×10^{-4}	3.83	935	80	This work
$Cu_{0.66}Co_{0.34}$–CeO_2–Pt	0.995	7.24×10^{-6}	2.00×10^{-4}	1.88	882	51.2	This work
$Cu_{0.50}Co_{0.50}$–CeO_2–Pt	0.633	7.22×10^{-6}	2.00×10^{-4}	3.46	480	98.8	This work
$Cu_{0.34}Co_{0.66}$–CeO_2–Pt	0.614	8.24×10^{-6}	2.00×10^{-4}	3.17	459	99.2	This work
$Co_{1.00}$–CeO_2–Pt	0.555	2.05×10^{-5}	2.00×10^{-4}	3.66	160	97.8	This work
CeO_2–Pt	0.285	2.09×10^{-5}	2.00×10^{-4}	6.15	93	89.9	This work
$Pt@CeO_2$	—	1.00×10^{-4}	1.00×10^{-3}	—	46	—	34
$Pt@CeO_2$/RGO	—	1.00×10^{-4}	1.00×10^{-3}	—	90	—	34

[a] M_{Pt}: mole of noble metals; $M_{4\text{-}NP}$: mole of 4-NP; t: conversion time; P: conversion percentage.

(Table 1). Though the most stable sample of $Cu_{0.50}Co_{0.50}$–CeO_2–Pt shows a moderate catalytic activity compared to others for catalytic 4-NP conversion, its TOF of 480 h^{-1} is still at least five times higher than our previously reported $Pt@CeO_2$ catalysts.[34]

Good reproducibility and stability are also important for the evaluation of catalysts. In order to avoid the loss of the Cu_x-Co_{1-x}–CeO_2–Pt catalysts caused by the separation process, cycling tests have been conducted *in situ*. Fig. 7B shows the conversion in successive reaction cycles of the Cu_xCo_{1-x}–CeO_2–Pt catalysts, and the conversions of 4-NP for the fifth cycle are listed in Table 1. It is found that the stability of the samples varied with the compositions of different doping ions, and that the Co rich samples show better stability among these catalysts.

Besides, catalytic CO oxidation was employed to evaluate these catalysts. In the catalytic process, the gas mixture of CO and O_2 was introduced into the inner space of a stainless steel reaction tube filled with Cu_xCo_{1-x}–CeO_2–Pt catalysts. T_{100}, the temperature for 100% CO oxidation, is used to compare the catalytic activity of these samples. Despite of the minor difference in the doped components, these samples show quite different catalytic performance. Fig. 8 presents their CO conversion curves, and the T_{100} values follow a sequence of: $Cu_{0.50}Co_{0.50}$–CeO_2–Pt (90 °C) < $Cu_{0.66}Co_{0.34}$–CeO_2–Pt (120 °C) < Co–CeO_2–Pt (125 °C) < CeO_2–Pt (135 °C) < Cu–CeO_2–Pt (140 °C) < $Cu_{0.34}Co_{0.66}$–CeO_2–Pt (155 °C). It can be seen that the catalytic

performance of our samples improves with the increase in the doping amount of Co until the ratio of $Cu^{2+}/Co^{2+} = 0.5/0.5$ is reached, and then this deteriorates quickly upon the doping of more Co^{2+} ions. This result indicates that Cu^{2+} and Co^{2+} ions can replace the tetravalent Ce^{4+} in the CeO_2 fluorite lattice to produce more oxygen vacancies, but an appropriate doping ratio of Cu^{2+}/Co^{2+} ions is needed in order to realize optimal catalytic performance in our case.

Conclusions

We have successfully prepared a series of Cu_xCo_{1-x}–CeO_2–Pt hybrid nanospheres. Based on detailed characterization including SEM, TEM, XPS, ICP and XRD, it is found that (I) in the nucleation process, the introduction of Cu^{2+} accelerated the nucleation rate compared with CeO_2, leading to the formation of the smaller sized CeO_2. (II) The Cu^{2+} doping concentration can affect the amount of Pt nanoparticles deposited to a greater extent than Co^{2+}. With the increase in Cu^{2+} doping concentration, the amount of Pt nanoparticles on the Cu_xCo_{1-x}–CeO_2 nanospheres decreases. However, the related effect of Cu^{2+} ions was quite small. (III) The high purity of all products indicates the formation of homogeneous Ce–Cu–Co–O, Ce–Cu–O or Ce–Co–O solid solutions.

Based on the catalytic tests, it is also found that the doping amount of Cu^{2+} greatly influences the catalytic performance of the Cu_xCo_{1-x}–CeO_2 nanospheres. Though the most stable sample of $Cu_{0.50}Co_{0.50}$–CeO_2–Pt shows a moderate catalytic activity compared to others for catalytic 4-NP conversion, its TOF of 480 h^{-1} is still much higher than our previously reported $Pt@CeO_2$ catalysts. Moreover, among the Cu_xCo_{1-x}–CeO_2–Pt samples, the $Cu_{0.50}Co_{0.50}$–CeO_2–Pt nanospheres exhibited the best catalytic activity, attaining 100% CO conversion at 90 °C, which is also higher than previously reported Pt catalysts. It can be anticipated that this kind of double doped nanocatalysts will have great potential for application.

Acknowledgements
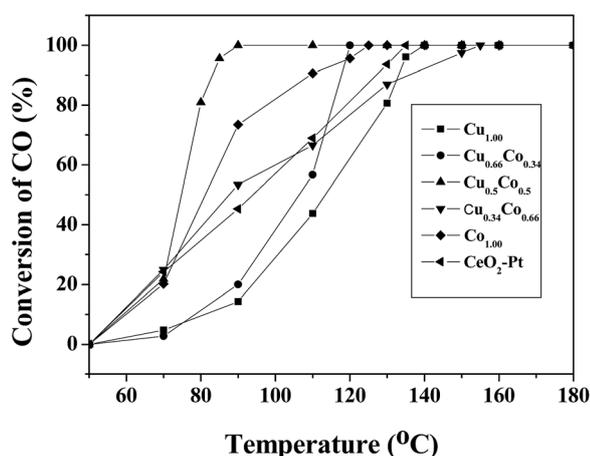
Fig. 8 CO conversion curves of Cu_xCo_{1-x}–CeO_2–Pt and CeO_2–Pt.

Notes and references

1 S. Sen, T. Edwards, S. K. Kim and S. Kim, *Chem. Mater.*, 2014, **26**, 1918–1924.

2 M. Zeng, Y. Z. Li, M. Y. Mao, J. L. Bai, L. Ren and X. J. Zhao, *ACS Catal.*, 2015, **5**, 3278–3286.

3 D. Jiang, W. Z. Wang, L. Zhang, Y. L. Zheng and Z. Wang, *ACS Catal.*, 2015, **5**, 4851–4858.

4 W. Y. Lei, T. T. Zhang, L. Gu, P. Liu, J. A. Rodriguez, G. Liu and M. H. Liu, *ACS Catal.*, 2015, **5**, 4385–4393.

5 Y. X. Liu, X. C. Sun, B. K. Li and Y. Lei, *J. Mater. Chem. A*, 2014, **2**, 11651–11659.

6 J. Qi, J. Chen, G. D. Li, S. X. Li, Y. Gao and Z. Y. Tang, *Energy Environ. Sci.*, 2012, **5**, 8937–8941.

7 J. M. Zhen, X. Wang, D. P. Liu, S. Y. Song, Z. Wang, Y. H. Wang, J. Q. Li, F. Wang and H. J. Zhang, *Chem.–Eur. J.*, 2014, **20**, 1–6.

8 F. Wang, X. Wang, D. P. Liu, J. M. Zhen, J. Q. Li, Y. H. Wang and H. J. Zhang, *ACS Appl. Mater. Interfaces*, 2014, **6**, 22216–22223.

9 X. Wang, D. P. Liu, J. Q. Li, J. M Zhen and H. J. Zhang, *NPG Asia Mater.*, DOI: 10.1038/am.2014.128.

10 J. K. Edwards, J. Pritchard, L. Lu, M. Piccinini, G. Shaw, A. F. Carley, D. J. Morgan, C. J. Kiely and G. J. Hutchings, *Angew. Chem., Int. Ed.*, 2014, **53**, 2381–2384.

11 L. L. Wang, H. Huang, S. H. Xiao, D. P. Cai, Y. Liu, B. Liu, D. D. Wang, C. X. Wang, H. Li, Y. R. Wang, Q. H. Li and T. H. Wang, *ACS. Appl. Mater. Interfaces*, 2014, **6**, 14131–14140.

12 P. F. Xu, R. B. Yu, H. Ren, L. B. Zong, J. Chen and X. R. Xing, *Chem. Sci.*, 2014, **5**, 4221–4226.

13 K. Zhao, J. Qi, S. L. Zhao, H. J. Tang, H. J. Yin, L. B. Zong, L. Chang, Y. Gao, R. B. Yu and Z. Y. Tang, *Chin. J. Catal.*, 2015, **36**, 261–267.

14 K. Anupriya, E. Vivek and B. Subramanian, *J. Alloys Compd.*, 2014, **590**, 406–410.

15 P. Li, Y. Zhou, Z. Y. Zhao, Q. F. Xu, X. Y. Wang, M. Xiao and Z. G. Zou, *J. Am. Chem. Soc.*, 2015, **137**, 9547–9550.

16 K. Zhao, J. Qi, H. J. Yin, Z. M. Wang, S. L. Zhao, X. Ma, J. W. Wan, L. Chang, Y. Gao, R. B. Yu and Z. Y. Tang, *J. Mater. Chem. A*, 2015, **3**, 20465–20470.

17 J. Qi, K. Zhao, G. D. Li, Y. Gao, H. J. Zhao, R. B. Yu and Z. Y. Tang, *Nanoscale*, 2014, **6**, 4072–4077.

18 E. Aneggi, V. Rico-Perez, C. D. Leitenburg, S. Maschio, L. Soler, J. Llorca and A. Trovarelli, *Angew. Chem., Int. Ed.*, 2015, **54**, 1–5.

19 S. Snana, V. Esposito, J. W. Andreasen, J. Hjelm, W. Zhang, T. Kasama, S. B. Simonsen, M. Christensen, S. Linderoth and N. Pryds, *Nat. Mater.*, 2015, **14**, 500–504.

20 S. P. S. Badwal, D. Fini, F. T. Ciacchi, C. Munnings, J. A. Kimptonb and J. Drennan, *J. Mater. Chem. A*, 2013, **1**, 10768–10782.

21 J. A. Rodriguez, S. Ma, P. Liu, J. Hrbek, J. Evans and M. Pérez, *Science*, 2007, **318**, 1757–1759.

22 D. Jiang, W. Z. Wang, E. Gao, S. M. Sun and L. Zhang, *Chem. Commun.*, 2014, **50**, 2005–2007.

23 X. Liang, X. Wang, Y. Zhuang, B. Xu, S. Kuang and Y. D. Li, *J. Am. Chem. Soc.*, 2008, **130**, 2736–2737.

24 M. Mogensen, N. M. Sammes and G. A. Tompsett, *Solid State Ionics*, 2000, **129**, 63–94.

25 D. Zhang, X. Du, L. Shi and R. Gao, *Dalton Trans.*, 2012, **41**, 14455–14475.

26 G. K. Reddy, G. Thrimurthulu and B. M. Reddy, *Catal. Surv. Asia*, 2009, **13**, 237–255.

27 D. N. Durgasri, T. Vinodkumar, P. Sudarsanam and B. M. Reddy, *Catal. Lett.*, 2014, **144**, 971–979.

28 Y. X. Zhao, Z. W. Nie, M. M. Shi, C. H. Zeng, Y. Li, L. Wang and S. L. Zhong, *Inorg. Chem. Front.*, 2015, **2**, 567–575.

29 B. W. Lu, Y. W. Ju, T. Abe and K. Kawamoto, *Inorg. Chem. Front.*, 2015, **2**, 741–748.

30 A. Trovarelli, *Comments Inorg. Chem.*, 1999, **20**, 263–284.

31 Y. Tang, H. Zhang, L. Cui, C. Ouyang, S. Shi, W. Tang, H. Li, J. S. Lee and L. Chen, *Phys. Rev. B: Condens. Matter Mater. Phys.*, 2010, **82**, 125104–125112.

32 J. M. Zhen, D. P. Liu, X. Wang, J. Q. Li, F. Wang, Y. H. Wang and H. J. Zhang, *Dalton Trans.*, 2015, **44**, 2425–2430.

33 X. Wang, D. P. Liu, S. Y. Song and H. J. Zhang, *J. Am. Chem. Soc.*, 2013, **135**, 15864–15872.

34 Y. R. Zheng, M. R. Gao, H. H. Li, Q. Gao, M. N. Arshad, H. A. Albar, T. R. Sobahi and S. H. Yu, *Science China Materials*, 2015, **58**, 179–185.

35 C. G. Hu, Q. Han, F. Zhao, Z. Y. Yuan, N. Chen and L. T. Qu, *Science China Materials*, 2015, **58**, 21–27.

36 X. Wang, D. P. Liu, J. Q. Li, J. M. Zhen, F. Wang and H. J. Zhang, *Chem. Sci.*, 2015, **6**, 2877–2884.

37 D. P. Liu, W. Li, X. L. Feng and Y. Zhang, *Chem. Sci.*, 2015, **6**, 7015–7019.

38 T. Yu, J. Zeng, B. Lim and Y. N. Xia, *Adv. Mater.*, 2010, **22**, 5188–5192.

39 H. P. Zhou, H. S. Wu, J. Shen, A. X. Yin, L. D. Sun and C. H. Yan, *J. Am. Chem. Soc.*, 2010, **132**, 4998–4999.

40 K. Yoon, K. Yang, P. Lu, D. Wan, H. Peng, K. Masias, P. Fanson, C. Campbell and Y. N. Xia, *Angew. Chem., Int. Ed.*, 2012, **51**, 9543–9546.

41 Y. Y. Chu, Z. B. Wang, Z. Z. Jiang, D. M. Gu and G. P. Yin, *Adv. Mater.*, 2011, **23**, 3100–3104.

42 N. M. Schweitzer, J. A. Schaidle, O. K. Ezekoye, X. Q. Pan, S. Linic and L. T. Thompson, *J. Am. Chem. Soc.*, 2011, **133**, 2378–2381.

43 G. Postole, B. Chowdhury, B. Karmakar, K. Pinki, J. Banerji and A. Auroux, *J. Catal.*, 2010, **269**, 110–121.

44 W. Liu, X. F. Liu, L. J. Feng, J. X. Guo, A. R. Xie, S. P. Wang, J. C. Zhang and Y. Z. Yang, *Nanoscale*, 2014, **6**, 10693–10700.

45 S. M. El-Sheikh, A. A. Ismail and J. F. Al-Sharab, *New J. Chem.*, 2013, **37**, 2399–2407.

46 M. Huang, Y. X. Zhang, F. Li, Z. C. Wang, Alamusi, N. Hu, Z. Y. Wen and Q. Liu, *Sci. Rep.*, DOI: 10.1038/srep04518.